CrystEngComm

PAPER

View Article Online
View Journal | View Issue

Cite this: *CrystEngComm*, 2018, **20**, 6046

High contrast mechanochromic and thermochromic luminescence switching by a deep red emitting organic crystal†

Manas K. Panda, *[ab] Nayana Ravi,[a] P. Asha[c] and A. P. Prakasham[d]

Received 29th April 2018,
Accepted 26th June 2018

DOI: 10.1039/c8ce00696b

rsc.li/crystengcomm

In this study, we report a deep red emissive organic crystal that displays high contrast fluorescence switching under mechanical and thermal stimulation. Upon mechanical grinding, the pristine red emissive crystals of **1R** (λ_{em} = 667 nm) transformed into green emissive crystalline powder (λ_{em} = 550 nm) with a remarkable hypsochromic shift of wavelength, $\Delta\lambda$ = 117 nm. The melting of **1R** leads to a green emissive amorphous solid (λ_{em} = 555 nm) with a wavelength shift of $\Delta\lambda$ = 112 nm. Upon fuming with different solvents, the amorphous melt solid transforms into different polymorphs having distinct emission characters. The structural relationship between different emissive states is investigated with the aid of X-ray diffraction and other spectroscopic studies, which clearly demonstrate the roles of ordered molecular packing and intermolecular interaction in determining their diverse optical response.

Introduction

Solid materials that change photoluminescence (PL) color in response to external stimuli are of great interest for optoelectronic devices,[1–3] sensors,[4,5] memory recording,[6] security writing,[7,8] and solid-state lasers.[9,10] In recent years, a large number of mechano-, thermo- or vapo-responsive photoluminescent materials have been developed and explored for various applications. Although inorganic-based dyes such as Pt-, Au-, and Ir-complexes have rich and diverse emission properties,[11–18] organic-based solid emitters have recently been getting more attraction primarily because of their low toxicity, low cost of raw materials and light weight.

Mechanochromic luminescent (MCL) materials have recently attracted immense attention because of fundamental curiosity about their mechanisms as well as their various applications. Developing materials that exhibit high contrast PL color in two different solid states have been a great challenge since it needs considerable changes in electronic interactions in the photoexcited state. Such emission switching in solid crystalline materials relies on the reconfiguration of molecular packing and/or conformational changes in response to external stimuli. Except for a few handful of examples that show high contrast color switching,[19–21] most of the organic-based MCL materials display small energetic shifts which are usually towards the bathochromic end.[22–30] Examples of organic materials that exhibit hypsochromic luminescence with a large wavelength shift in response to mechanical or other stimuli are rather limited.[31–33] From a point of fundamental interest, developing such organic materials have attracted immense attention because, in this way, one can produce high energy emission by mechanically stimulating the low energy emissive material. This calls for the design and synthesis of red or NIR emissive materials which is another challenging task, because these materials are generally made of long π-conjugated molecules or macrocyclic aromatics and are prepared by multistep synthesis followed by tedious purification process. One alternative way to achieve small molecular red-emissive materials is to introduce a suitable donor–acceptor functionality in the molecule that favors strong intramolecular and intermolecular charge transfer interactions in the solid state which lowers the optical band gap and results in red/NIR emission. Such a strategy has been recently adopted by Kim *et al.* and Cheng *et al.*[34,35]

Herein, we report a deep red emissive organic crystal (**1R**) that exhibits a large hypsochromic luminescence shift from red to green upon application of mechanical and thermal stimuli. Mechanical grinding of the red emissive crystal **1R** (λ_{max} = 667 nm) leads to green emissive powder (**1R**-grind, λ_{max} = 550 nm) with a remarkably large wavelength shift, $\Delta\lambda$ =

[a] *Photosciences & Photonics Section, Chemical Science & Technology Division, CSIR-National Institute for Interdisciplinary Science & Technology, Thiruvananthapuram, Kerala-695019, India. E-mail: mannup25@gmail.com, manas.panda@niist.res.in*
[b] *Academy of Scientific and Innovative Research (AcSIR), New Delhi 110025, India*
[c] *School of Chemistry, Indian Institute for Science and Educational Research, Thiruvananthapuram, Kerala-695551, India*
[d] *Department of Chemistry, Indian Institute of Technology Bombay, Mumbai-400076, India*

† Electronic supplementary information (ESI) available: X-ray crystallographic CCDC number 1840350 (**1R**). For ESI and crystallographic data in CIF or other electronic format see DOI: 10.1039/c8ce00696b

117 nm. Melting of the **1R** crystal also results in a green emissive material (**1R**-melt, λ_{max} = 555 nm) with an energy shift of 112 nm. To our knowledge, this is one rare example of a single molecular component organic crystal that displays such a large hypsochromic fluorescence shift within the visible color spectrum. The molecular components of **1** include donor diphenylamine (DPA) and acceptor $Ph(CF_3)_2$ functional groups which favor strong intramolecular charge transfer interactions both in solution and in the solid state. Compound **1** is highly emissive in the solid state due to the strongly allowed electronic transition between delocalized frontier molecular orbitals in the densely packed molecular environment. Our design strategy offers a much simpler synthesis to achieve deep red emission in the solid state and could have potential application in low-cost optoelectronic devices.

Experimental section

Materials and methods

3,5-Bis(trifluoromethyl)phenylacetonitrile was purchased from TCI India and 4-(diphenylamino)benzaldehyde (DPA) was purchased from Sigma-Aldrich and were used without further purification. Tetrabutyl ammonium hydroxide (TBAH) was purchased from Merck Chemicals and was used as received. HPLC grade solvents were used for crystallization and spectroscopy studies.

Instruments

Absorption and fluorescence spectra. Solution state UV-vis spectra were recorded on a Shimadzu UV-Vis 2600 spectrophotometer and solid-state absorption spectra were recorded on a PerkinElmer Lambda 35 UV-vis spectrophotometer using an integrating sphere. For the UV-vis analysis of the **1R** crystal, a few small sized crystallites were attached to a quartz plate and placed in the optical path during data collection. In the case of **1R**-grind, a thin film was made on the quartz plate by careful grinding the **1R** crystal. Solid state emission spectra of the crystals and ground samples were recorded using a HORIBA SPEX Fluorolog FL-1039 spectrofluorometer. The smaller sized crystals or ground samples were glued (with non-fluorescent grease) on the sample holder groove and covered with a quartz disc and then the spectra were recorded. For the absolute quantum yield (QY) measurement, the crystals and ground samples were sandwiched between two glass plates and placed in the optical path inside a calibrated integrating sphere in a HORIBA Fluorolog spectrofluorometer (SPEX) employing a Xe arc lamp as the excitation source in the sphere using specific excitation wavelengths. Prior to the experiment, the integrating sphere was calibrated using tris(8-hydroxyquinolinato) aluminum (Alq3). The absolute quantum yield was calculated using a method reported previously.[36] Fluorescence lifetime measurements were carried out using a modular time correlated single photon counting spectrometer (Horiba) equipped with a DeltaFlex detector: PPD850.

Optical microscopy. Fluorescence images were captured using a Leica DM 2500P microscope. For the temperature dependence study, a Linkam THMS 600 hot stage was used which is equipped with a microscope.

IR spectroscopy. Infrared spectra were recorded using a SHIMADZU IR Prestige-21 spectrometer using KBr as the matrix.

Thermal study. Differential scanning calorimetric (DSC) measurements were carried out using a TA Instruments DSC Q2000 model with a refrigerated cooling system with a heating and cooling rate of 10 °C min^{-1} under a nitrogen atmosphere. Thermogravimetric analyses (TGA) were performed using a TA instruments SDT Q600 V20.9 Build 20 with a heating rate of 10 °C per minute using nitrogen as the purging gas.

Powder X-ray diffraction (PXRD). PXRD data of the samples were measured using a XEUSS SAXS/WAXS system by Xenocs, operated at 50 kV and 0.60 mA. The X-ray radiation was collimated with a FOX2D mirror and two pairs of scatterless slits from Xenocs. The data were collected in the transmission mode geometry using Cu Kα radiation (wavelength λ = 1.54 Å). The fiber diagrams were recorded using an image plate system (mar345 detector) and processed using Fit2D software.

Single-crystal X-ray diffraction. The data of the crystals were collected using a Bruker APEX-II CCD diffractometer at 298 K using graphite-monochromated MoKα radiation (λ = 0.71073 Å). The SAINT software was used for data reduction, which were analyzed for agreement using XPREP.[37] Absorption correction was carried out using the SADABS program.[38] The structure was determined by the method included in the SHELXT program of the APEX software suite and refined using SHELXL-2014.[39–42] The non-hydrogen atoms were refined anisotropically. The positions of the hydrogen atoms were calculated and refined isotropically. Details of the crystallographic parameters are given in ESI† Table S3. The crystallographic data have been deposited with the Cambridge Crystallographic Data Centre (CCDC) under reference no. 1840350.

Computational methods. Density functional theory (DFT) calculations were carried out using the Gaussian 09 program suite using a hybrid Becke three-parameter exchange functional combined with the Lee–Yang–Parr correlation functional (B3LYP).[43–45] The 6-31G(d) basis set was used for all calculations. Gas-phase geometry optimizations of the monomer and dimer were performed using coordinates from the crystal structure of **1R**. In the case of the model dimer, two parallel stacked molecules were chosen from the packing diagram and geometrically optimized in the gas phase. Single point calculations were carried out in both the gas phase and in the solvent phase (DMF). Tomasi's polarizable continuum model (PCM)[46] was used for describing the solvent effect on the HOMO–LUMO gap of the compound. All of the output structures were visualized using the Chemcraft software.[47]

Synthesis procedure

The compound was synthesized by following a reported method.[48] Briefly, to a solution of 4-(diphenylamino)-

benzaldehyde (0.230 g, 0.84 mmol) in 20 mL methanol, 3,5-bis(trifluoromethyl)phenylacetonitrile (0.15 mL, 0.84 mmol) was added. Subsequently, potassium *tert*-butoxide (0.112 g, 1.0 mmol) and tetrabutyl ammonium hydroxide (1 mL, 1.0 mmol, 25% w/v methanol solution) was added to the reaction pot and the resulting solution was heated at 50 °C for 4 h. The product mixture was cooled and kept for crystallization for 2 days. Orange coloured plate-shaped crystals of the product were obtained from the mother liquor which was isolated by filtration (0.321 g, 75%). ^{1}H NMR (500 MHz, $CDCl_3$): δ (ppm) 8.05 (s, 2H, Ar-*H*), 7.83 (d, 3H, J = 8 Hz, Ar-*H*), 7.51 (s, 1H, Ar-*H*), 7.35 (t, 4H, J = 8 Hz, Ar-*H*), 7.19–7.15 (m, 6H, Ar-*H*), 7.05 (d, 2H, J = 8 Hz, Ar-*H*). HRMS: calculated for $C_{29}H_{18}F_6N_2$ is 508.1374, obtained m/z = 509.1452 (M + H).

Results and discussion

Photophysical characterization

Molecular compound **1** (Fig. 1a) was synthesized by the reaction between 4-(diphenylamino)benzaldehyde and 3,5-bis(trifluoromethyl)phenylacetonitrile in 75% yield, following a literature procedure.[48] The compound was thoroughly characterized by spectroscopic and single crystal X-ray diffraction studies. The UV-vis spectra of **1** (in DMF or toluene solution, 1×10^{-5} M) display a strong absorption band with λ_{max} = 415 nm which can be assigned to the intramolecular charge transfer (ICT) interaction involving the donor–acceptor group in the molecule (Fig. 1c).

The density functional theory (DFT) study of the monomer species revealed that the HOMO is concentrated on the diphenylamine donor while the LUMO is located on the CF_3-substituted phenyl ring acceptor, which is also supportive of the ICT character (Fig. 1b and d and S1, ESI†). The steady state fluorescence spectra of **1** in toluene solution (1×10^{-6} M) exhibits an emission band at λ_{max} = 522 nm which corresponds to the ICT fluorescence (^{1}CT → S_0 transition) of the monomer species. This band is red-shifted in DMF solution to λ_{max} = 612 nm (Stokes shift of 7756 cm^{-1}) due to the solvatochromic effect (Fig. 1c). The time-resolved fluorescence spectra of **1** in toluene solution showed a single exponential decay with a lifetime of 0.304 ns (λ_{em} = 523 nm) which corresponds to the monomeric species. Interestingly, compound **1** shows aggregation-induced emission enhancement (AIEE) behavior. As depicted in Fig. S2b, ESI,† upon addition of water to the DMF solution of **1** (1×10^{-3} M), the emission intensity drastically increases with a concomitant blue-shift of the emission maxima. This AIE effect could be ascribed to the presence of bulky twisted phenyl rings of the diphenylamine moiety that favor a non-planar arrangement during the aggregation process and prevent the non-radiative loss of excited state energy. Moreover, the blue shift of the emission maxima can be attributed to the random arrangement of molecules in the aggregate state (**1**-aggregate) which disallows long range electronic delocalization. Along this line, we have also tested the emission behavior of aggregates from a dilute solution of a volatile solvent. As observed from Fig. S2a, ESI,† the drop-casted aggregated film of **1** (1×10^{-4} M in dichloromethane solution) exhibits green emission with λ_{max} = 543 nm. Our visual inspection reveals that these are bead-like spherical particles and not crystalline.

Slow evaporation of the hot DMF solution of **1** produced deep red emissive crystals **1R** which display a broad absorption profile peaking at ~440 nm. This band could be attributed to the charge transfer band in the solid state (Fig. S2a, ESI†). Compared to those in the solution spectra, the broadening and slight red shift of the solid-state absorption band can be attributed to the delocalized charge transfer state which lowers the optical band gap. In fact, the spectroscopic band gap calculation reveals that the HOMO–LUMO gap in the crystalline state (2.01 eV) is much lower than in that in the solution state (2.43 eV in DMF solution), further supporting the above statement. In order to observe FMO distribution, DFT calculation was carried out for a dimeric species where two molecules are in close proximity (using the input coordinates from the crystal structure of **1R**). As shown in Fig. S1b, ESI,† the electron density of the HOMO is located on the donor moiety of one molecule while the LUMO density is located on the acceptor group of another molecule, indicating intermolecular charge transfer interaction with a concomitant decrease in the HOMO–LUMO gap (compared to that in a monomer). Accordingly, the solid state fluorescence spectra of the **1R** crystal exhibit a structureless emission band with a maximum at λ_{max} = 667 nm (Fig. S2a, ESI†) which is significantly red shifted (by 55 nm) compared to that in DMF solution. Such a large red shifted emission is expected to be contributed by an electronic excited state that arose from delocalized frontier molecular orbitals favored by intermolecular interaction between the molecules in orderly packed crystalline media. In fact, the solid state excitation spectra of the **1R** crystal (λ_{em} monitored at 660 nm) showed a red shifted ICT band along with a new shoulder band at 580 nm which can be assigned to intermolecular charge transfer interaction in the solid crystal matrix (Fig. S3, ESI†). The

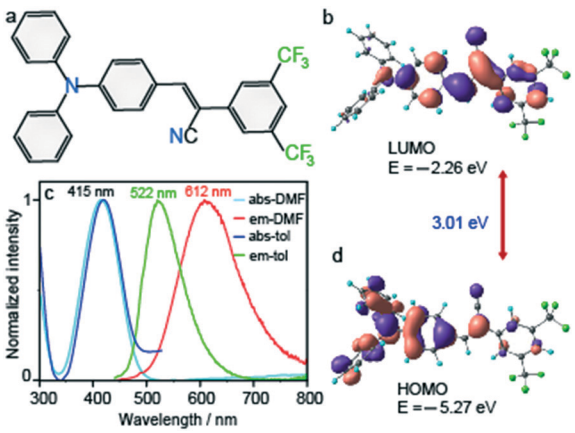

Fig. 1 (a) Molecular structure of **1**; (b and d) frontier molecular orbitals (FMO) of **1** obtained from DFT calculations; (c) absorption and emission spectra of **1** in toluene and DMF solution.

pristine **1R** crystals are highly emissive in nature having a solid state quantum yield of 0.50, which is much higher than that in DMF solution. (Table S1, ESI†). The enhanced quantum yield can be attributed to the crystallization induced emission enhancement (CIEE) resulting from the combined effect of stronger ICT and long range intermolecular interactions in the crystal that restrict the conformation flexibility and minimize the non-radiative loss of excited energy.[49] It is interesting to observe that an ordered aggregation/assembly in the crystal leads to a bathochromic emission shift (**1** in DMF solution *vs.* the **1R** crystal) while a random aggregation leads to a hypsochromic emission shift (**1** in DMF solution *vs.* **1**-aggregate in the DMF–water mixture). This observation indicates the key role of molecular arrangement in facilitating the delocalization of the charge transfer excited state in solid media that can tune the emission colour.

The time resolved emission profile of the **1R** crystal exhibits a tri-exponential decay curve with lifetimes (τ) of 25.5 ns (41%), 7.3 ns (50%), and 0.48 (8.4%), suggesting that there might be a competitive radiative pathway through which the excited molecules relax in the crystal (Table S2, ESI†). These values are higher than the lifetimes observed in the solution state, presumably because of the stabilization of excited states due to various intermolecular interactions in the crystalline matrix.

Single crystal X-ray structure

The red emissive **1R** crystallizes in the monoclinic system with a $P2_1$ space group (Fig. 2, Table S3, ESI†). Two antiparallel molecules in the asymmetric unit are stabilized by intermolecular C–H···π interaction involving a DPA proton and the phenyl ring of the acceptor group of the other molecule (H6 to centroid distance = 3.245 Å, Fig. 2a). Conformational analysis of the molecules in the asymmetric unit reveals that the π-phenyl ring and acceptor phenyl rings are nearly coplanar (14.53°, Fig. 2b). However, the phenyl rings of the donor DPA group are much more twisted and the dihedral angles between the π-phenyl plane and the DPA phenyl planes are 67.34° and 57.59°. Such a conformation would prevent a closer approach of the molecules in packed solid media. In fact, as depicted in Fig. 2c, the distance between two phenyl planes of slip-stacked parallel molecules is 5.268 Å (centroid to centroid distance) which impedes intermolecular π···π stacking interaction and thereby prevents fluorescence quenching in the solid state (Fig. S4, ESI†). The molecules are packed in a parallel fashion on the *ac* plane and connected by C–H···N hydrogen bonding interactions (H43···N4 = 2.657 Å, H14···N2 = 2.684 Å) as well as C–H···π interactions (H to centroid distance = 3.495 Å, Fig. 2). Interestingly, as shown in Fig. S5, ESI,† the molecules are alternatively connected by C–H···F and C–H···π interactions in a manner that facilitates the intermolecular charge transfer interaction between the donor group of one molecule and the acceptor group of the other molecule. This long-range delocalization of charge transfer interaction is one of the possible factors for the red emission of the **1R** crystal. This interaction is extended like a zigzag chain along the crystallographic *b*-axis. As mentioned earlier, the shoulder band at 580 nm in the fluorescence excitation spectra is due to the newly generated excited state that corresponds to intermolecular charge transfer interaction in the crystal (Fig. S3, ESI†). Furthermore, our DFT calculation of the dimer shows that the HOMO is located on the donor group of one molecule while the LUMO is primarily concentrated on the acceptor group of the other molecule, indicating the occurrence of intermolecular charge transfer interaction that lowers the HOMO–LUMO energy gap (Fig. S1b†).

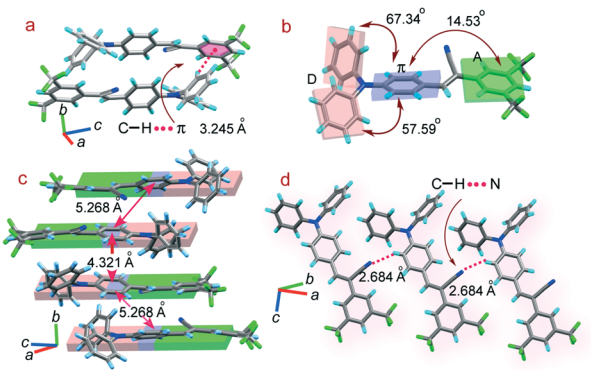

Fig. 2 Crystal structure of **1R** (a) interaction between two molecules in an asymmetric unit; (b) twist angles between the phenyl planes; (c and d) stacking and intermolecular interactions in **1R** along different crystallographic directions.

Mechanochromic luminescence

Interestingly, **1R** crystals display impressive mechanochromic and thermochromic luminescence switching with a remarkable shift in fluorescence wavelength. Upon gentle crushing (with a mortar and pestle), the red emissive crystal turns into bright yellow emissive fragments having λ_{max} = 580 nm (Fig. 3a and c). Further grinding leads to a greenish yellow emissive material (**1R**-grind) having λ_{max} = 550 nm with an overall wavelength shift of $\Delta\lambda$ = 117 nm (Fig. 3b and e). Such a large shift of wavelength is rarely observed, particularly for molecular organic materials. Upon fuming with common organic solvents (hexane, dichloromethane, chloroform, methanol, THF, DMF, *etc.*), the green emissive **1R**-grind transformed into the yellow emissive form, but not into the red emissive form. The PXRD pattern of the green emissive **1R**-grind confirms that the material retains its crystallinity after grinding. However, compared to the pristine **1R** crystal, the reflection peaks are much broader for **1R**-grind, suggesting a decrease in long range molecular order in the later (Fig. 3d). As observed from Fig. S6, ESI,† several diffraction peaks of **1R** in the higher 2θ region (20–30°) disappeared or have drastically reduced intensity upon grinding. This observation is supportive of pressure induced structural rearrangement to a relatively disordered phase in **1R**-grind. Such diminution of

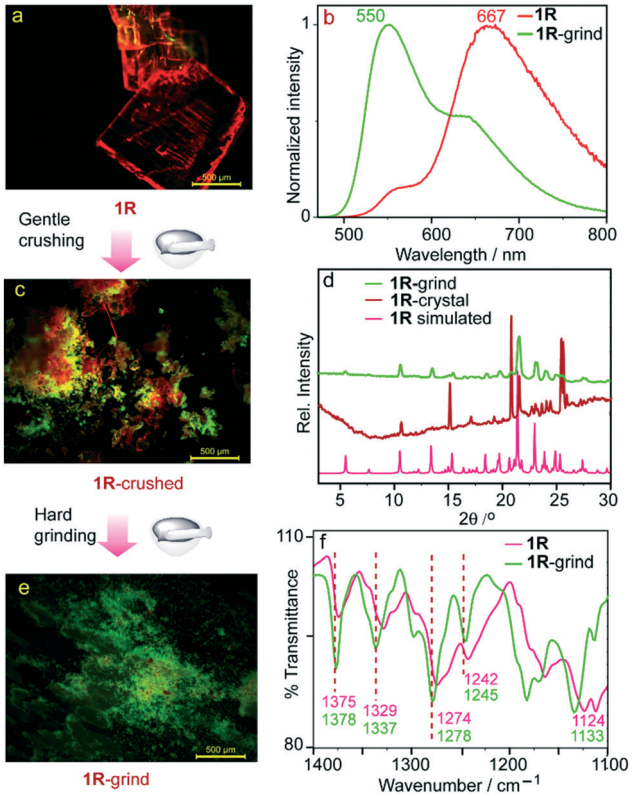

Fig. 3 Mechanochromic luminescence switching of a pristine **1R** crystal; (a, c and e) fluorescence microscopy images at different stages of grinding; (b) emission spectra of **1R** and **1R**-grind; (d) PXRD plots; (f) infrared spectra of **1R** and **1R**-grind.

the long range order would result in perturbation of intermolecular charge transfer interaction. Indeed, as observed from Fig. S3, ESI,† the excitation band at 580 nm which corresponds to intermolecular charge transfer interaction disappears upon grinding. In this stage, the monomeric ICT interaction is expected to be dominant which results in the green emission of **1R**-grind peaking at λ_{em} = 550 nm. It is important to mention here that, during the crystallization of the red emissive **1R**, we have also observed the formation of a few pieces of micron sized green emissive polymorphs (Fig. S7, ESI†). These crystals are very much fragile and difficult to handle. Our repeated attempts to scale up the crystallization of green polymorphs and to obtain good diffraction quality crystals were unsuccessful.

To unravel the molecular level change during the course of mechanochromic switching, we have carried out infrared spectroscopy on the pristine **1R** crystal (ATR spectra) and ground powder (**1R**-grind). Comparative analysis of the spectra indicates that the degree of intermolecular interaction is very much perturbed upon grinding. Specifically, the out of plane aromatic C–H frequencies in **1R**, 890 and 841 cm^{-1}, blue shifted to 893 and 843 cm^{-1} in **1R**-grind (Fig. S8, ESI†), suggesting the change in symmetry as well as the weakening of the intermolecular interactions such as C–H···N and C–H···π involving this bond. Moreover, the symmetric and asymmetric CF_3 stretching frequencies 1124, 1329 and 1374 cm^{-1} (Fig. 3f) in **1R** also increase upon grinding, suggesting a significant change in the hydrogen bonding interactions involving this functional group. Such weakening of intermolecular interaction in the solid state would result in the loss of crystallinity and long-range order which is also reflected in the PXRD pattern of **1R**-grind (discussed earlier).

Thermochromic luminescence

In order to explore the thermochromic luminescence of **1R**, we first carried out thermogravimetric analysis (TGA) and differential thermal calorimetry (DSC). As shown in Fig. S9 and S10, ESI,† the pristine crystal **1R** is thermally stable up to ~200 °C and has a melting point of 134.7 °C. The melting point slightly decreased upon grinding due to the loss of intermolecular contacts in **1R**-grind. Next, we heated the **1R** crystal (heating rate 10 °C per minute) on a Linkam hot stage equipped with a fluorescence microscope. Upon heating, the crystal loses its fluorescence near the melting point; however, it regains a weak green fluorescence (λ_{max} = 555 nm) upon cooling to room temperature (Fig. 4a and d). The difference in emission wavelength between the **1R** crystal and cooled solid melt (**1R**-melt) is 112 nm, nearly in the same range as that observed upon grinding (Fig. 4j). The PXRD plots of **1R**-melt reveals a featureless pattern which confirms its amorphous nature (Fig. 4k). This suggests that the molecules in **1R**-melt are devoid of long-range intermolecular interactions that can affect the electronic state delocalization, and as a

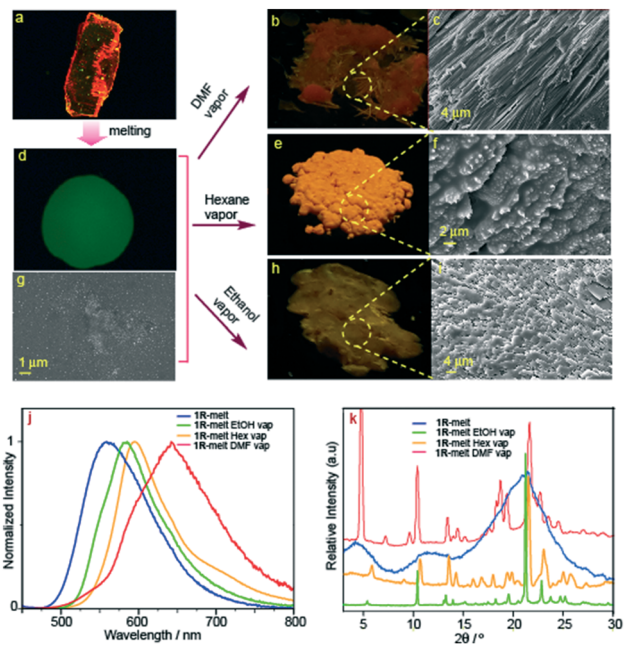

Fig. 4 (a and d) Fluorescence microscopic images of **1R** and **1R**-melt, respectively; (b, e and h) fluorescence microscopy images of recrystallized materials upon fuming of **1R**-melt with DMF, hexane and ethanol vapor, respectively; (c, f and i) the corresponding SEM images; (g) SEM image of **1R**-melt; (j) emission spectra and (k) PXRD plots of **1R**-melt and solvent fumed recrystallized materials.

result, it exhibits green emission due to monomeric ICT fluorescence.

Interestingly, when the amorphous **1R**-melt was exposed to solvent vapor fuming, it recovers its crystallinity with a concomitant increase in fluorescence intensity. A diverse range of fluorescence colors was observed with different solvents. For example, fuming of the green emissive **1R**-melt with DMF vapor (at 50 °C) resulted in a crystalline solid having a structureless orange-red emission band which has a λ_{max} of 650 nm and a broad shoulder in the orange region (Fig. 4b and j). A comparison between the emission spectra (Fig. 3b and 4j) and PXRD patterns (Fig. 3d and 4k) suggest that the vapour fumed orange-red phase (*i.e.* **1R**-melt DMF vap) and the pristine red emissive phase, **1R** are different. Fuming of **1R**-melt with ethanol vapor (at 60 °C) results in yellow emissive crystalline materials (λ_{max} = 584 nm) while fuming with hexane (at 40 °C) results in yellowish-orange emissive (λ_{max} = 594 nm) crystalline materials. Such distinct emission colors could arise due to the formation of different polymorphic forms induced by solvent vapor molecules having different polarities. Scanning electron microscopy (SEM) analysis of the solvent fumed crystalline materials reveals unique morphologies of the crystallites that have different emission behaviors (Fig. 4c, f and i). The DMF fumed red emissive materials are needle-shaped while the yellow emissive crystallites are plate-shaped. In fact, the PXRD patterns of these vapor fumed crystallites confirmed their different molecular packings (Fig. 4k). As observed from Fig. 4k, these polymorphs feature many sharp peaks, indicating the formation of well-ordered crystalline structures.

A comparative look on the PXRD patterns of the pristine **1R** crystal and vapour fumed polymorphs (Fig. S11, ESI†) reveal that the patterns are relatively dissimilar, except for a few common reflection peaks at 2θ = 10.4° and 21.6°. This difference in packing can be rooted to the crystallization processes of **1R** (by slow evaporation) and vapor fumed crystallites (fast vapour fuming).

The TGA thermograms of the recrystallized samples do not show any weight change related to solvent loss which confirms that no solvent molecules are trapped in the lattice (Fig. 5a). Thus, possibly solvent molecules of different sizes and polarities interact with the disordered molecules of **1** in the amorphous solid and induce reordering or relaxation into different types of packings that have distinct photophysical features. In order to shed more light into the molecular level changes, we have obtained the infrared spectra of the amorphous **1R**-melt and solvent fumed crystallized materials which provide important information about the changes in intermolecular interactions. As depicted in Fig. 5b, the symmetric CF_3 stretching frequencies at 1136 and 1337 cm^{-1} in **1R**-melt are downshifted to 1133 and 1333 cm^{-1}, respectively, indicating the re-engagement in intermolecular interactions upon crystallization.

Based on all the above observations, we propose a mechanistic model that could demonstrate the structure–emission correlation of the solid state emissive behavior of **1** (Fig. 5c). The molecules in the **1R** crystal are orderly connected to each

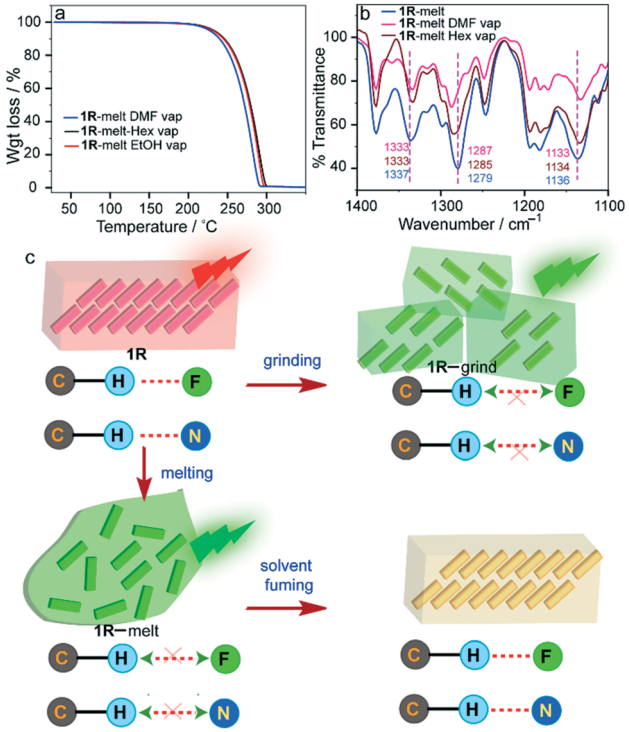

Fig. 5 (a) TGA thermograms of vapor fumed recrystallized materials; (b) infrared spectra of **1R**-melt and vapor fumed crystallized samples showing changes in stretching frequency upon crystallization; (c) cartoon model of the structural change and the corresponding emission behavior.

other by non-covalent interactions that facilitate the delocalization of charge transfer interactions and this results in red emission. Upon hard grinding of the crystal, the long-range order of the molecules is perturbed which inhibits the delocalization of charge transfer interaction and thus exhibits a hypsochromically shifted ICT emission of the isolated molecule. Melting of **1R** also leads to a disordered amorphous state where intermolecular interactions between the molecules are insignificant and results in green emission that corresponds to the ICT interaction.

Conclusion

In summary, we have developed a synthetically simple cyanostyryl-based deep red emitting organic crystal that exhibits remarkably high-contrast fluorescence switching. The emission colors of **1** in the solid state can be effectively tuned by external stimuli such as pressure, temperature and solvent vapour fuming to modulate the molecular packing. With the aid of single crystal X-ray diffraction and spectroscopic characterization, we have unraveled the molecular level mechanism that is responsible for structural switching during this fluorochromism. In the solution state, green emission is caused by ICT interaction within the molecule where it exists as isolated monomeric species, whereas, the tightly packed ordered orientation of molecules in the **1R** crystal facilitates the delocalization of charge transfer states by various

intermolecular interactions and results in deep red emission. Upon mechanical or thermal stimulation, the tight packing structure of **1R** is loosened, its molecules become disordered, thus weakening the intermolecular interactions that affect the delocalization of the electronic excited state, and as a result, blue-shifted emission occurs. On the other hand, vapor fuming of amorphous molecules (melt solid) induce reordering of molecules in different packing arrangements that result in distinct fluorescent phases with bathochromically shifted emission. Such a concept design of the present molecule could be exploited further to develop new deep red/NIR emissive materials that might exhibit exotic luminescence properties and can be used for novel optoelectronic applications.

Conflicts of interest

There are no conflicts to declare.

Acknowledgements

M. K. P. thanks the Council of Scientific and Industrial Research (CSIR, Govt of India) for the fellowship and the director of CSIR-NIIST for providing facilities.

Notes and references

1 M. Shimada, M. Tsuchiya, R. Sakamoto, Y. Yamanoi, E. Nishibori, K. Sugimoto and H. Nishihara, *Angew. Chem., Int. Ed.*, 2016, **55**, 3022–3026.
2 S. K. Park, J. H. Kim, S. J. Yoon, O. K. Kwon, B. K. An and S. Y. Park, *Chem. Mater.*, 2012, **24**, 3263–3268.
3 G. M. Farinola and R. Ragni, *Chem. Soc. Rev.*, 2011, **40**, 3467–3482.
4 C. Bariain, I. R. Matias, I. Romeo, J. Garrido and M. Laguna, *Appl. Phys. Lett.*, 2000, **77**, 2274–2276.
5 S. H. Lim, L. Feng, J. W. Kemling, C. J. Musto and K. S. Suslick, *Nat. Chem.*, 2009, **1**, 562–567.
6 S. Hirata, K. Lee and T. Watanabe, *Adv. Funct. Mater.*, 2008, **18**, 2869–2879.
7 R. Thirumalai, R. D. Mukhopadhay, V. K. Praveen and A. Ajayaghosh, *Sci. Rep.*, 2015, **5**, 09842, DOI: 10.1038/srep09842.
8 H. Sun, S. Liu, W. Lin, K. Y. Zhang, W. Lv, X. Huang, F. Huo, H. Yang, G. Jenkins, Q. Zhao and W. Huang, *Nat. Commun.*, 2014, **5**, 3601, DOI: 10.1038/ncomms4601.
9 X. Cheng, K. Wang, S. Huang, H. Zhang, H. Zhang and Y. Wang, *Angew. Chem., Int. Ed.*, 2015, **54**, 8369.
10 A. Camposeo, M. Polo, P. D. Carro, L. Silvestri, S. Tavazzi and D. Pisignano, *Laser Photonics Rev.*, 2014, **8**, 785.
11 J. R. Kumpfer, S. D. Taylor, W. B. Connick and S. J. Rowan, *J. Mater. Chem.*, 2012, **22**, 14196–14204.
12 X. Zhang, J.-Y. Wang, J. Ni, L.-Y. Zhang and Z.-N. Chen, *Inorg. Chem.*, 2012, **51**, 5569–5579.
13 T. Seki, T. Ozaki, T. Okura, K. Asakura, A. Sakon, H. Uekusa and H. Ito, *Chem. Sci.*, 2015, **6**, 2187–2195.
14 M. Jin, T. Seki and H. Ito, *J. Am. Chem. Soc.*, 2017, **139**, 7452.
15 T. Seki, K. Kobyashi and H. Ito, *Chem. Commun.*, 2017, **53**, 6700–6703.
16 M. Jin, T. Sumitani, H. Sato, T. Seki and H. Ito, *J. Am. Chem. Soc.*, 2018, **140**, 2875–2879.
17 M. Mydlak, C. Bizzarri, D. Hartman, W. Sarfert, G. Schmid and L. De Cola, *Adv. Funct. Mater.*, 2010, **20**, 1812–1820.
18 S. Lamansky, P. Djurovich, D. Murphy, F. Abdel-Razzaq, H. E. Lee, C. Adachi, P. E. Burrows, S. R. Forrest and M. E. Thompson, *J. Am. Chem. Soc.*, 2001, **123**, 4304–4312.
19 H.-J. Kim, D. R. Whang, J. Gierschner, C. H. Lee and S. Y. Park, *Angew. Chem., Int. Ed.*, 2015, **54**, 4330–4333.
20 Y. Sagara and T. Kato, *Angew. Chem., Int. Ed.*, 2011, **50**, 9128–9132.
21 Y. Sagara, Y. C. Simon, N. Tamaoki and C. Weder, *Chem. Commun.*, 2016, **52**, 5694–5697.
22 B. R. Crenshaw, M. Burnworth, D. Khariwala, A. Hiltner, P. T. Mather, R. Simha and C. Weder, *Macromolecules*, 2007, **40**, 2400–2408.
23 Y. Sagara, K. Kubo, T. Nakamura, N. Tamaoki and C. Weder, *Chem. Mater.*, 2017, **29**, 1273–1278.
24 J. Wu, Y. Cheng, J. Lan, D. Wu, S. Qian, L. Yan, Z. He, X. Li, K. Wang, B. Zou and J. You, *J. Am. Chem. Soc.*, 2016, **138**, 12803–12812.
25 P. Rajamalli, P. Gandeepan, M.-J. Huang and C.-H. Cheng, *J. Mater. Chem. C*, 2015, **3**, 3329–3335.
26 J. Wang, Z. Liu, S. Yang, Y. Lin, Z. Lin and Q. Ling, *Chem. – Eur. J.*, 2018, **24**, 322–326.
27 P. S. Hariharan, E. M. Mothi, D. Moon and S. P. Anthony, *ACS Appl. Mater. Interfaces*, 2016, **8**, 33034–33042.
28 Y. Sagara, S. Yamane, M. Mitani, C. Weder and T. Kato, *Adv. Mater.*, 2016, **28**, 1073–1095.
29 P. Xue, P. Chen, J. Jia, Q. Xu, J. Sun, B. Yao, Z. Zhang and R. Lu, *Chem. Commun.*, 2014, **50**, 2569–2571.
30 M. Li, Q. Zhang, J. Wang and X. Mei, *Chem. Commun.*, 2016, **52**, 11288–11291.
31 P.-Z. Chen, J.-X. Wang, L.-Y. Niu, Y.-Z. Chen and Q.-Z. Yang, *J. Mater. Chem. C*, 2017, **5**, 12538–12546.
32 K. Nagura, S. Saito, H. Uasa, H. Yamawaki, H. Fujihisa, H. Sato, H. Shimoikeda and S. Yamaguchi, *J. Am. Chem. Soc.*, 2013, **135**, 10322–10325.
33 M. Tanioka, S. Kamino, A. Muranaka, Y. Ooyama, H. Ota, Y. Shirasaki, J. Horigome, M. Ueda, M. Uchiyama, D. Sawada and S. Enomoto, *J. Am. Chem. Soc.*, 2015, **137**, 6436–6439.
34 M. Kim, D. R. Whang, J. Gierschner and S. Y. Park, *J. Mater. Chem. C*, 2015, **3**, 231–234.
35 X. Cheng, K. Wang, S. Huang, H. Zhang, H. Zhang and Y. Wang, *Angew. Chem., Int. Ed.*, 2015, **54**, 8369–8373.
36 J. C. deMello, H. F. Wittmann and R. H. Friend, *Adv. Mater.*, 1997, **9**, 230–232.
37 APEX DUO, version 2.1–4, and SAINT, version 7.34A, Bruker AXS Inc., Madison, WI, 2012, URL: https://www.bruker.com.
38 G. M. Sheldrick, *SADABS*, University of Göttingen, Göttingen, Germany, 1996.
39 G. M. Sheldrick, *SHELXL2014*, University of Göttingen, Göttingen, Germany, 2014.

40 G. M. Sheldrick, *SHELXTL XT – Crystal Structure Solution, version 2014/4*, Bruker AXS, 2010–2014.
41 G. M. Sheldrick, *Acta Crystallogr., Sect. A: Found. Crystallogr.*, 2015, **71**, 3–8.
42 G. M. Sheldrick, *Acta Crystallogr., Sect. A: Found. Crystallogr.*, 2008, **64**, 112–122.
43 M. J. Frisch, G. W. Trucks, H. B. Schlegel, G. E. Scuseria, M. A. Robb, J. R. Cheeseman, G. Scalmani, V. Barone, B. Mennucci, G. A. Petersson, H. Nakatsuji, M. Caricato, X. Li, H. P. Hratchian, A. F. Izmaylov, J. Bloino, G. Zheng, J. L. Sonnenberg, M. Hada, M. Ehara, K. Toyota, R. Fukuda, J. Hasegawa, M. Ishida, T. Nakajima, Y. Honda, O. Kitao, H. Nakai, T. Vreven, J. A. Montgomery Jr., J. E. Peralta, F. Ogliaro, M. Bearpark, J. J. Heyd, E. Brothers, K. N. Kudin, V. N. Staroverov, R. Kobayashi, J. Normand, K. Raghavachari, A. Rendell, J. C. Burant, S. S. Iyengar, J. Tomasi, M. Cossi, N. Rega, J. M. Millam, M. Klene, J. E. Knox, J. B. Cross, V. Bakken, C. Adamo, J. Jaramillo, R. Gomperts, R. E. Stratmann, O. Yazyev, A. J. Austin, R. Cammi, C. Pomelli, J. W. Ochterski, R. L. Martin, K. Morokuma, V. G. Zakrzewski, G. A. Voth, P. Salvador, J. J. Dannenberg, S. Dapprich, A. D. Daniels, Ö. Farkas, J. B. Foresman, J. V. Ortiz, J. Cioslowski and D. J. Fox, *Gaussian 09, revision A.02*, Gaussian, Inc., Wallingford, CT, 2009.
44 A. D. Becke, *Phys. Rev. A: At., Mol., Opt. Phys.*, 1988, **38**, 3098–3100.
45 C. Lee, W. Yang and R. G. Parr, *Phys. Rev. B: Condens. Matter Mater. Phys.*, 1988, **37**, 785–789.
46 M. Cossi, V. Barone, R. Cammi and J. Tomasi, *Chem. Phys. Lett.*, 1996, **255**, 327–335.
47 http://www.chemcraftprog.com.
48 A. Adak, T. Panda, A. Raveendran, K. S. Bejoymohandas, K. S. Asha, A. P. Prakasham, B. Mukhopadhyay and M. K. Panda, *ACS Omega*, 2018, **3**, 5291–5300.
49 J. Gierschner and S. Y. Park, *J. Mater. Chem. C*, 2013, **1**, 5818–5832.